



Alluvial record of an early Eocene hyperthermal, Castissent Formation, Pyrenees, Spain

Louis Honegger¹, Thierry Adatte², Jorge E. Spangenberg³, Jeremy K. Caves Rugenstein⁴, Miquel Poyatos-Moré⁵, Cai Puigdefabregas⁶, Emmanuelle Chanvry⁷, Julian Clark⁸, Andrea Fildani⁸, Eric Verrechia², Kalin Kouzmanov¹, Matthieu Harlaux¹, Sébastien Castellort¹

¹Department of Earth Sciences, University of Geneva, Rue des Maraîchers 13, 1205 Geneva, Switzerland

²Institut of Earth Sciences, Géopolis, University of Lausanne, 1015 Lausanne, Switzerland

10 ³Institute of Earth Surface Dynamics (IDYST), Géopolis, University of Lausanne, 1015 Lausanne, Switzerland

⁴Geological Institute, ETH Zürich, Sonneggstrasse 5 NO E61, 8092 Zürich, Switzerland

⁵Department of Geosciences, University of Oslo, Sem Sælands vei 1, 0371 Oslo, Norway

⁶Department of Earth and Ocean Dynamics, University of Barcelona, C/ Martí i Franquès, s/n, 08028 Barcelona, Spain

15 ⁷University of Poitiers & CNRS, IC2MP, INC, 86000 Poitiers, France

⁸Equinor Research Center, 6300 Bridge Point Parkway, Building 2, Suite 100, Austin, Texas, USA

Correspondence to: Louis Honegger (louis.honegger@unige.ch)

20 **Abstract.** During the late Palaeocene to the middle Eocene (57.5 to 46.5 Ma) a total of 39 hyperthermals—
periods of rapid global warming recorded by prominent negative carbon isotope excursions (NCIEs) as well as
peaks in iron content—have been recognized in marine cores. Understanding how the Earth system responded to
rapid warming during these hyperthermals is fundamental because they represent potential analogues, in the
geological record, to the ongoing anthropogenic modification of global climate. However, while hyperthermals
25 have been well documented in the marine sedimentary record, only few have been recognized and described in
continental deposits, thereby limiting our ability to understand the effect and record of global warming on
terrestrial surficial systems. Hyperthermals in the continental record could be a powerful correlation tool to help
connect marine and continental records, addressing issues of environmental signal propagation from land to sea.
In this study, we generate new stable carbon isotope data ($\delta^{13}\text{C}$ values) across the well-exposed and time-
30 constrained fluvial sedimentary succession of the early Eocene Castissent Formation in the South-Central
Pyrenees (Spain). The $\delta^{13}\text{C}$ values of pedogenic carbonate reveal—similarly to the global records—stepped
NCIEs, culminating in a minimum $\delta^{13}\text{C}$ value that we correlate with the hyperthermal event “U” at *ca.* 50 Ma.
This general trend towards more negative values is most probably linked to higher primary productivity leading
to an overall higher respiration of soil organic matter during these climatic events. The relative enrichment in
35 immobile elements (Zr, Ti, Al) and higher estimates of mean annual precipitation together with the occurrence of
small iron-oxides/hydroxides nodules during the NCIEs suggest intensification of chemical weathering and/or
longer exposure of soils in a highly seasonal climate. The results show that even relatively small-scale
hyperthermals compared with their prominent counterparts, such as PETM, ETM2 and 3, have left a
recognizable trace in the stratigraphic record, providing insights into the dynamics of the carbon cycle in
40 continental environments during these events.



1 Introduction

Starting at the end of the Palaeocene, a period of global warming reached its climax during the Early Eocene Climatic Optimum (EECO) (Hyland and Sheldon, 2013; Westerhold and Röhl, 2009). The EECO started *ca.* 53 Ma ago and lasted until *ca.* 49 Ma ago (Westerhold et al., 2018), after which the climate began to cool towards icehouse conditions eventually reached later in the Cenozoic (~Eocene-Oligocene transition, Zachos et al., 2001, 2008). Superimposed on, and coeval to, this globally warm epoch, brief-periods of pronounced global warming known as “hyperthermals” stand out as anomalies outside of background climate variability (Dunkley Jones et al., 2018; Turner et al., 2014). The Palaeocene-Eocene Thermal Maximum (PETM; ~56 Ma) was the first of these events to be identified globally because of its exceptional magnitude and preservation in both marine and continental deposits (Koch et al., 1992). To date, for the late Paleocene – early Eocene period, a total of 39 hyperthermal events of lesser magnitude have been identified from marine cores (e.g., Westerhold et al., 2018), among which the most prominent and studied are the Early Thermal Maximum (ETM) 2, H2, I1, I2, and ETM3/X events (Deconto et al., 2012; Lourens et al., 2005; Lunt et al., 2011; Nicolo et al., 2007; Turner et al., 2014) (Fig. 1). In the stratigraphic record, these events are primarily characterized by important negative carbon isotope excursions (NCIEs) exceeding background variability (Abels et al., 2016; Cramer et al., 2003; Lauretano et al., 2016; Nicolo et al., 2007; Sluijs and Dickens, 2012; Zachos et al., 2008), i.e. typically with amplitude greater than the standard deviation (SD) of pre-hyperthermal background values.

In deep marine settings, the NCIEs are typically paired with an increase in iron concentration and decrease in carbonate content, indicating ocean acidification potentially linked with high atmospheric CO₂ concentrations (Nicolo et al., 2007; Slotnick et al., 2012; Westerhold et al., 2018). In coastal marine sections, Early Eocene hyperthermal events are generally associated with an enhanced flux of terrigenous material, interpreted as linked to accelerated hydrological cycle and higher seasonality (Bowen et al., 2004; Dunkley Jones et al., 2018; Nicolo et al., 2007; Payros et al., 2015; Slotnick et al., 2012), although several studies document a spatially heterogeneous hydrological climatic response during the PETM (Bolle and Adatte, 2001; Carmichael et al., 2017; Kraus and Riggins, 2007). In fluvial systems, the abrupt warming of the PETM was found to be associated with expansion and coarsening of alluvial facies combined with an increase of the magnitude of flood discharge (Chen et al., 2018; Foreman et al., 2012; Pujalte et al., 2015), as well as enhanced pedogenesis (Abels et al., 2012). Yet, how continental systems reacted to the other, smaller-magnitude hyperthermals of the Early Eocene remains to be documented. In particular, because of the subaerial nature and important lateral dynamics of alluvial systems (e.g., Foreman and Straub, 2017; Straub and Foreman, 2018), the extent to which fluvial successions can provide complete and faithful archives of past climatic events, especially those with the smallest magnitudes, is a matter of debate (Foreman and Straub, 2017; Straub and Foreman, 2018; Trampush et al., 2017). Addressing this question is particularly critical for studies attempting to understand environmental signal propagation in source-to-sink system (e.g., Castellort and Van Den Driessche, 2003; Duller et al., 2019; Romans et al., 2016; Schlunegger and Castellort, 2016), which require high-resolution continental-marine correlations such as those provided by the PETM (e.g., Duller et al., 2019) but also by other hyperthermals of the Early Eocene.

To address these issues, we explored some aspects of the geochemical signature (carbon and oxygen stable isotopes, major and trace elements) and of the sedimentology of the fluvial Castissent Fm (South-Central Pyrenees, Spain, Fig. 2), whose deposition took place during the late EECO. First, we generated a new carbon



isotope profile from a paleosol succession rich in carbonate nodules across the Castissent Fm in order to compare these results with a global $\delta^{13}\text{C}$ record. The data suggest that this fluvial succession preserves a record of hyperthermal “U” event at *ca.* 50 Ma, adding important constraints to the age of this Formation. Second, we used the major and trace element composition of bulk floodplain material in order to explore the climatic impact of such minor hyperthermal, including empirical reconstructions of mean annual precipitation, allowing us to discuss soil dynamics during global warming. This study identifies for the first time in a continental succession an event so far only recorded in marine sediments, thereby demonstrating the global breadth of these climatic events and the complementarity of oceanographic and terrestrial archives.

2 Geological setting

90 The Castissent Formation is a Ypresian age fluvial Formation that crops out in the Tremp-Graus Basin (South-Pyrenean foreland basin, Marzo et al., 1988, Fig. 2), which developed during the Paleocene to Eocene and is bounded by the Bóixols thrust in the North, and the Montsec thrust in the South (Marzo et al., 1988). The Castissent Fm is defined by its prominent overall sand-rich character, and is composed in detail of three coarse-grained multistorey channels complexes (labelled as Members A, B and C) separated by four marine incursions
95 (M0 to M3) inferred from the observation of marginal coastal bioclast-rich horizons developed up into the upper deltaic plain and correlative with finer dark-grey mudstones and calcretes in the fluvial segment of the Castissent (Marzo et al., 1988). This major fluvial progradation is correlated westwards with deep-water turbidite sequences of the Arro and Fosado Formations in the Ainsa Basin (Fig. 3, Mutti et al., 1988; Nijman and Nio, 1975; Nijman and Puigdefabregas, 1978; Pickering and Bayliss, 2009). In the upstream, eastern counterparts of the Castissent
100 Fm, the channel complexes are intercalated with yellow to red coloured paleosols. Sub-spherical to slightly elongated carbonate nodules with a diameter ranging from 1 mm to 4 cm are omnipresent in the paleosols. Studies of the Castissent Fm tentatively attributed its occurrence to an important pulse of exhumation and thrust activity in the hinterland at *ca.* 50 Ma, in possible combination with a late-Ypresian sea-level fall (Castelltort et al., 2017; Marzo et al., 1988; Puigdefabregas et al., 1986; Whitchurch et al., 2011), both resulting in reduced
105 available accommodation space enhancing progradation and amalgamation (Chanvry et al., 2018).

Constraints on the age of the Castissent Fm in its upstream segment is the recognition of European Mammals zone MP10 (Checa-Soler, 2004; Payros and Tosquella, 2009), which gives a broad age range of between 50.73 to 47.4 Ma (GTS2012). However, most age constraints have been obtained through bio- and magnetostratigraphic studies in the downstream more marine-influenced segment of the Castissent Fm in the
110 Campo area located 40km westward from the Chiriveta section (fig. 3). Thanks to its very prominent field expression, the Castissent Fm has been physically mapped from west to east across these sections (Nijman, 1998; Nijman and Nio, 1975; Poyatos-Moré, 2014) and the stratigraphic constraints obtained in the west can thus be propagated eastwards to its more fluvial counterparts (Fig. 3). Kapellos and Schaub (1973) find the transition between the *D. lodoensis* and the *T. orthostylus* nannoplankton (NP) zones at *ca.* 200 m below the base of the
115 Castissent Fm and the transition between the *T. orthostylus* and the *D. sublodoensis* NP zones in the transgression *ca.* 100 m above the uppermost Member of the Castissent Fm. This indicates that the Castissent Fm was deposited during NP13. Magnetostratigraphic data of the same section by Bentham and Burbank (1996) place the transition between C22r and C22n magnetozones closely above the top of the Castissent Fm. We thus used the recent astrochronologic age models of Westerhold et al. (2017), which obtain numerical ages of



120 50.777±0.01 and 49.695±0.043 Ma respectively for the base and top of C22r, and obtain a numerical age of
50.534±0.025 Ma for the base of NP13 based on ODP site 1263. We considered that these constraints give a
maximal age extension of between 50.534±0.025 and 49.695±0.043 Ma for the Castissent Fm (reported in green
on fig. 1). According to global isotopic records (Fig. 1), this period was marked by 4 hyperthermals labelled S,
T, U and V (Lauretano et al., 2016; Westerhold et al., 2017).

125 **3 Material and methods**

The Chiriveta section is situated in a continental paleogeographic position prone to pedogenesis and slightly off-axis from the more “in-axis” amalgamated sand-rich type section of Mas de Faro (Fig. 2); for paleo-position and correlation see also Figs. 10 and 12 in Marzo et al. (1988).

3.1 Sampling

130 A total of 74 samples were collected from the early-Eocene Chiriveta section for geochemical studies. All
samples consist of floodplain material and were taken below the weathering depth (~50 cm), with an average
resolution of 1 m. Resolution was increased by a factor of 2 in specific horizons such as red beds. When
important sandbodies occurred, lateral equivalent floodplain material or intercalated paleosol horizons were
sampled. Each sample was split in two aliquots, one for major and trace element analysis and the other for
135 carbon and oxygen stable isotope analysis on pedogenic carbonate nodules. The carbonate nodules were
extracted from the bulk paleosol material by sieving and then cleaned by repeated washes with deionized water
in an ultrasound bath. From each cleaned nodules set, subsamples of 1 to 4 nodules were taken, leading to a total
of 149 sub-samples of pedogenic carbonate nodules.

3.2 Carbon and oxygen stable isotopes

140 Pedogenic carbonate nodules were crushed and powdered in an agate mortar and analysed for stable carbon and
oxygen isotope composition at the Institute of Earth Surface Dynamics of the University of Lausanne
(Switzerland) using a Thermo Fisher Scientific (Bremen, Germany) carbonate-preparation device and Gas Bench
II connected to a Thermo Fisher Delta Plus XL isotope ratio mass spectrometer. The carbon and oxygen isotope
compositions are reported in the delta (δ) notation as the per mil (‰) isotope ratio variations relative to the
145 Vienna Pee Dee Belemnite standard (VPDB). The analytical reproducibility estimated from replicate analyses of
the international calcite standard NBS-19 and the laboratory standard Carrara Marble was better than ± 0.05 ‰
(1 sigma) for $\delta^{13}\text{C}$ and ± 0.1 ‰ (1 sigma) for $\delta^{18}\text{O}$.

3.3 Major and trace element composition

Fifty-two bulk paleosol samples were analysed for major and trace elements using X-Ray fluorescence (XRF)
150 spectrometry. Crushed bulk powders (<80 μm) were mounted in a plastic cup covered by a thin polypropylene
film (4 μm thick) and analysed in the laboratory with a Thermo Niton XL3t® portable XRF analyzer fixed on a
test stand. Analyses were performed with a beam diameter of 8 mm, to determine the concentrations of 34 major
and trace elements (from Mg to Au). Each measurement took 120 s, consisting of two 60 s cycles on four
different filters (15 seconds on low, main, high, and light ranges), operating the X-ray tube at different voltage to



155 optimize the fluorescence and peak/background ratios of the different elements. The limits of detection were of
10's ppm for most elements, except for Mg, Si, and Al which are at wt% level. Na is too light to be detected. The
spectra of the measurements were transferred to a computer using NDT software version 8.2.1. (Thermo Fisher
Scientific, Waltham, Ma, USA). Twenty-three major and trace elements were analysed on pressed and fused
discs of the same material using a PANalytical PW2400 XRF spectrometer at the University of Lausanne to
160 cross-calibrate the compositions measured with the Niton XL3t@ portable XRF analyzer.

3.4 Mean annual precipitation

The mean annual precipitation estimate (MAP) used in this study was estimated from the empirical relationship
between MAP and CaO/Al₂O₃ ratio for Mollisols from a national survey of North American soils according to
the following equation: MAP (mm) = -130.9*ln(CaO/Al₂O₃) + 467 (Sheldon et al., 2002). CaO and Al₂O₃
165 concentrations were measured on bulk paleosol material. Climate linked to the MAP estimate was classified
based on the following boundaries: arid to semiarid at 250 mm and semiarid to subhumid at 500 mm (Bull,
1991).

3.5 Grain-size estimation

The relative grain-size variation of the sediment samples was estimated from their major element compositions.
170 Si, Ti and Zr are more concentrated in the coarse fraction of the sediment as they are found in larger mineral
grains, whereas Al is more concentrated in the finer fraction of the sediment because is mostly linked to clay
minerals (Croudace and Rothwell, 2015; Lupker et al., 2011, 2012). Grain size variation throughout the section
was estimated using Si/Al, Ti/Al and Zr/Al ratios, therefore, an increase in these ratios suggests a relative
increase in the proportion of coarser material in the sample.

175 3.6 Correlation with target curves

The measured $\delta^{13}\text{C}$ dataset was compared with a time-equivalent ODP 1263 global $\delta^{13}\text{C}$ record reported by
Westerhold et al. (2017) using the Anlyseries software (Paillard et al., 1996). The $\delta^{13}\text{C}$ record of site 1263 was
favoured over those of ODP 1209 and 1258 covering the Castissent Fm time-period, because it is continuous and
has a higher resolution. Correlations between the $\delta^{13}\text{C}$ record of site 1263 and the $\delta^{13}\text{C}$ record of the Chiriveta
180 section were performed in order to optimize the Pearson correlation coefficient (r) and by minimizing abrupt
variations in sedimentation rates. Well-defined peaks in both $\delta^{13}\text{C}$ records were used as tie-points for the
correlation and the number of tie-points was kept minimum (<10) so as not to force the correlations.

4 Results

4.1 Overview of the Castissent Fm at the Chiriveta section

185 In the proximal part of the Basin, the Castissent Fm is a paleosol rich succession, which shows greyish-yellow to
red-brown mottled floodplain paleosols (Fig. 4A-B-D-E), which correspond laterally to thick, medium to coarse-
grained quartz-rich channel-fill deposits (width/depth ratio = 20-50; Marzo et al. (1988)) and over-bank deposits
with an overall westerly flow direction parallel to the main structures of the growing Pyrenean orogeny (Marzo
et al., 1988). At the base of the section, the first marine incursion M0 is situated at the top of a 20 m-thick



190 coarse-grained tidal bar deposit with herringbone cross-stratifications and oyster shells (Fig. 4C). In the
Chiriveta section, the Castissent Member A is a 48 m-thick interval comprising two main white medium-grained
sandbodies of 5.40 and 1.5 m in thickness respectively. Sandy bed-forms observed in the first sandbody have a
mean height of 24 cm ($n = 9$). The second marine incursion M1 is located at 48 m just below the Castissent B
Member and consists of a 2 m-thick grey interval interpreted by Marzo et al. (1988) as poorly drained brackish
195 water facies (Fig. 4B-F). The Castissent B Member (Fig. 4G) begins with a 12 m-thick and laterally-extensive
(width/depth ratio ≥ 250 ; Marzo et al. (1988)) amalgamated sandbody with a micro-conglomeratic erosive base.
Grain size is overall larger than in Member A, and ranges from fine sand to large pebbles. Sandbodies tops show
a fining-upward trend and are capped by mottled siltstone packages. Mottled siltstone layers are interpreted as
pedogenized over-bank deposits based on roots traces and their capping relationship with underlying sandbody
200 deposits (observed at 26 m, 76 m, 89 m and 96 m in Fig. 4, Fig. 4H). More regular and sheet-like sandbodies
interbedded with several mottled siltstone layers are observed upwards. The section ends with a 23 m-thick,
medium to very coarse tidally-influenced sandstone deposits interpreted as the equivalent M3 marine incursion
by Marzo et al. (1988). Although Castissent Member C was not interpreted by Marzo et al. (1988) in this section,
a 2m-thick fine-grained sandbody at ca 80 meters on our section may be a condensed lateral equivalent of it (Fig.
205 5).

4.2 Stable isotopic record

Carbon and oxygen isotope ratios from the carbonate nodules are presented in Fig. 5. The $\delta^{13}\text{C}$ values vary
between -10.9 and -1.9‰ with a mean value and 1 SD of -7.7 ± 1.6 ‰. Six NCIE (named A to F in Fig. 5 and
colour coded in Fig. 6) are more negative than the mean value - 1 SD amongst which one (NCIE D) is below 2
210 SDs. The values are -9.6, -9.8, -9.9, -10.9, -9.9 and -9.4‰ for NCIEs A to F respectively. At the bottom of the
section, NCIE A is followed by a relatively constant interval of mean $\delta^{13}\text{C}$ values. NCIE B, situated in the first
red bed, marks the beginning of a stepped $\delta^{13}\text{C}$ trend (around ± 1 SD) leading to the minimum NCIE D. The
second part of the section shows two more NCIE separated by the highest $\delta^{13}\text{C}$ value at 65 m. NCIE F is the
lowest of all NCIEs. The $\delta^{18}\text{O}$ values vary between -7.0 and 5.0‰ with a mean value of -6.0 ± 0.4 ‰, which
215 makes them less dispersed than the $\delta^{13}\text{C}$ record. Nine negative oxygen isotope excursions (NOIEs) are more
negative than the mean value - 1 SD, amongst which one is below 2 SD reaching a minimum value of -6.8‰ at
19 m. The NOIEs do not correspond with NCIEs described above.

4.3 Major and trace elements

Titanium (Ti), Aluminium (Al) and Zirconium (Zr) concentrations measured on bulk paleosols are plotted in
220 Figure 5. These elements are commonly considered as immobile and are expected to concentrate in more
weathered soils. Ti values vary between 0.17 and 0.52% with a mean value of 0.34% and a standard deviation of
0.08. Al values vary between 3.57 and 9.89% with a mean value of 6.38% and a standard deviation of 1.53. Zr
values vary between 66 and 203 ppm with a mean value of 127 ppm and a standard deviation of 35. Mean annual
precipitation (MAP) estimates values vary between 205 and 755 mm/y with a mean value of 387 mm/y and a
225 standard deviation of 107. Ti, Al, Zr and MAP show a similar trend starting from the base of the section with a
global increase of all values toward NCIE C and a decrease afterwards. All NCIEs show higher value of Ti, Al,



Zr and MAP except NCIE F. Based on Bull (1991), an average value of 387 mm/y for the MAP in the Chiriveta section represent a semi-arid climate (Fig. 5). All NCIEs show an increase in MAP.

5 Discussion

230 5.1 Carbon and oxygen isotopic record

In continental successions, the carbon isotope composition of pedogenic carbonate nodules—which consists of calcareous concretions between 1 mm and 4 cm diameter formed *in situ* in the floodplain—have been proven to reflect global $\delta^{13}\text{C}$ variations (Abels et al., 2016; Koch et al., 1992; Schmitz and Pujalte, 2003), and may therefore be considered, sometimes together with the oxygen isotope composition ($\delta^{18}\text{O}$), as reliable proxy for
235 environmental condition occurring during their formation (e.g., Millièrè et al., 2011a, 2011b). The carbon isotope composition of the soil carbonate nodules depend on the $\delta^{13}\text{C}$ value of the soil CO_2 , which in turn is a function of the $\delta^{13}\text{C}$ of the atmospheric CO_2 , the overlying plants as well as soil respiration (Abels et al., 2012; Bowen et al., 2004; Cerling, 1984).

The $\delta^{13}\text{C}$ vs $\delta^{18}\text{O}$ diagram for the pedogenic carbonate nodules from the Chiriveta section ($r = -0.26$, $n = 149$)
240 suggests a good preservation of the primary isotopic signal (Figure 6), with an average value of $\delta^{13}\text{C} = -7.7 \pm 1.6$ ‰ similar to mid-latitude late-Palaeocene to Eocene continental $\delta^{13}\text{C}$ values (excluding the PETM samples) observed elsewhere (e.g., McInerney and Wing, 2011; and references therein), and a spread comparable with $\delta^{13}\text{C}$ values from carbonate nodule analysed for the same period in the Bighorn Basin (Bowen et al., 2001). Fig. 6 emphasizes that early-Eocene carbonate nodules display overall more negative $\delta^{13}\text{C}$ values than the Holocene
245 nodules, that is consistent with global data (Zachos et al., 2008). Pre-PETM $\delta^{18}\text{O}$ values from carbonate nodules from the same area (-4.5 ± 0.4 ‰) (Hunger, 2018) show similar range than those measured in the Chiriveta section (-6.0 ± 0.4 ‰). Moreover, the $\delta^{18}\text{O}$ values of soil carbonates from the Pyrenean foreland basin (excluding the PETM) (-5.3 ± 0.9 ‰) indicate a more coastal-influenced isotopic signature (Cerling, 1984) compared for example to those of the Bighorn Basin (-9.0 ± 0.6 ‰).

250 A hyperthermal event recorded in marine sediments is defined by a paired negative carbon and oxygen stable isotope excursions that are more negative than the mean value minus 1 SD (Turner et al., 2014). This definition may not be applicable to continental deposits, because continental systems respond differently than marine systems to the carbon cycle perturbations. Indeed, the $\delta^{13}\text{C}$ value of the marine dissolved inorganic carbon is influenced by dissolution of carbonates at depth (McInerney and Wing, 2011), whereas $\delta^{13}\text{C}$ in
255 pedogenic nodules vary with soil properties, atmospheric and soil $p\text{CO}_2$, the rate and nature of carbon input and/or output by soil respiration (Bowen et al., 2004; Sheldon and Tabor, 2009). These processes may cause a misleading estimation of CIE in soil carbonate nodules and in marine carbonates (McInerney and Wing, 2011). Nevertheless, we used Turner et al. (2014)'s hyperthermal definition as a starting point to filter the high-resolution variations in the Chiriveta section. 16 samples were identified with NCIE values more negative than
260 the mean -1 SD. Among these 16 samples, we recognized 6 discrete NCIEs (named A – F in Fig. 5 and 7). Both marine incursion M1 and M2 show an abrupt shift from -9 to -10 ‰ $\delta^{13}\text{C}$ values in continental towards more (positive) marine values of -4 to -2 ‰; this point to a progressive higher contribution of seawater to the formation of the carbonate nodules.



Six correlation options with the global record were explored in the time-window of the Castissent Fm
265 (Figure S1 and S2 in the Supplement). Correlation presented in Figure 7A was favoured for the following
reasons: i) it shows reasonable sedimentation rates variations, ii) is coherent with the NCIE amplitude of the
global record, and iii) it yielded the highest correlation coefficient ($r = 0.65$, $n = 71$). Moreover, it plots on the
same trend regarding hyperthermal NCIE amplitudes in marine and continental environments suggesting a
similar isotopic dynamic as events I1, I2, H2 and ETM2 (Figure 7B). Based on these observations and the
270 resulting correlation, we suggest that only hyperthermal U is preserved in the Chiriveta section and that it is
correlated with NCIE D. Sedimentation rate obtained with the favoured correlation (Figure 7) varies between
0.1-0.29 mm/y and the correlation coefficient of $r = 0.65$ suggests an overall good signal preservation in the
studied continental section for a 40 ky climatic event.

Soil organic matter sensitivity to a change in temperature is critical concerning today's global warming
275 (Melillo et al., 2014; Trumbore et al., 2006), because it represents two-thirds of the terrestrial carbon pool and
contains twice as much carbon as atmospheric CO₂ pool (Carrillo et al., 2018; Schimel et al., 1994). An increase
in temperature could therefore potentially release important amount of CO₂ into the atmosphere (Trumbore et al.,
2006). As the amplitude and duration of Eocene NCIEs are approximately 30% of the ones recorded in the
PETM, we hypothesize that the climatic effects of smaller-scale hyperthermals can be linearly scaled to the
280 PETM. Based on this assumption and in order to get a rough approximation without considering a non-linear
sensitivity response, a smaller-scale hyperthermal would imply a release of approximately 500 to 1500 Gt of
carbon to the ocean and atmosphere reservoir and a global temperature rise of about 1.5–2.5° C. This estimation
correspond to the 1500 – 4500 Gt of carbon released during the PETM, causing a rise of 5–8°C (Bowen et al.,
2006), and is in line with previous estimations of ~3 and ~2°C warming for ETM2/H1 and H2 events
285 respectively (Stap et al., 2010).

The $\delta^{13}\text{C}$ mean value in the Chiriveta section is -7.7 ± 1.6 ‰. This value reflects an overall equilibrium
with a mean atmospheric CO₂ of -7 ‰ (Koch et al., 1995) and is coherent with pre-PETM $\delta^{13}\text{C}$ values of $-7.1 \pm$
 0.9 ‰ found in the same area (Hunger, 2018; Fig. 6). It is possible to calculate from the (small-scale)
hyperthermal $\delta^{13}\text{C}$ excursions in the marine environment the shift to be expected in soil carbonate nodules by
290 using known fractionation coefficients (Koch et al., 1995, 2003); the expected $\delta^{13}\text{C}$ value in carbonate nodules,
only considering the respiration of organic matter, is of -11 ‰ (Fig. 8). This value is within the range of those
measured in Chiriveta section, where some nodules reach values as low as -10.9 ‰. We suggest that the bacterial
respiration of organic matter, enhanced by warmer temperatures (e.g.; Davidson and Janssens, 2006; Trumbore
et al., 2006), may also have contributed to the lower $\delta^{13}\text{C}$ values of nodules during the NCIEs (Fig. 8). On
295 geological timescales, soil organic carbon can be considered at steady state with equal organic carbon inputs and
outputs from the soil (Koven et al., 2017). Respiration (carbon output after mineralization as CO₂) is thought to
be more sensitive to global warming than gross primary productivity (organic carbon input as organic matter)
leading to a depletion of the total soil carbon pool with time during transient global warming events; although
the precise sensitivity of gross primary productivity remains poorly constrained (Davidson and Janssens, 2006).
300 Large uncertainties remain about carbon dynamics and their timescale in the soils during climate changes.
Parameters such as the vegetation type (Klemmedson, 1989), temperatures (Koven et al., 2017), soil
geochemistry (Doetterl et al., 2015; Torn et al., 1997), and soil water content (Davidson et al., 2000) have been
shown to be important controlling factors within historical timescales. Considering these caveats, we estimate



the maximum possible contribution of enhanced soil carbon respiration to negative $\delta^{13}\text{C}$ excursions during the
305 NCIEs. Using typical values for the organic carbon reservoir comprising fast and slow cycling carbon in soils in
arid to semi-arid ecosystems of 5.6–19.2 kgC/m² (Klemmedson, 1989; Raich and Schlesinger, 1992), respiration
fluxes starting at a steady state value of 0.5 kgC/y, and a respiration rate sensitivity *ca.* 5%/degree (Raich and
Schlesinger, 1992), we estimate that all of the organic carbon in soils would be consumed within 250 to 850 y,
given an increase of 1°C and without changing the carbon input rate. Though there are a number of assumptions
310 in this first-order estimate, the timescale of soil carbon depletion is substantially shorter than our estimate of the
timescale of the NCIE (~36 ky) (Fig. 7). As evidenced by this calculation, an increase in soil respiration
triggered by warmer temperatures cannot be the sole mechanism driving the NCIE shift over multi-millennial
time-scales. Instead, we suggest that during these transient warmings, this mechanism is associated with a high
primary productivity—resulting in a greater input of carbon to the soil—leading to an overall higher soil
315 respiration of organic matter. Coupled with lower atmospheric $\delta^{13}\text{C}$ during hyperthermals, this mechanism
caused a pronounced NCIE in soil carbonate nodules.

5.2 Geochemical signature of hyperthermal events

Major and trace elements compositions of floodplain sediments is a function of river dynamics, climate, and
sediment grain-size (Lupker et al., 2012; Turner et al., 2015). Based on the NCIE described above, we defined
320 six intervals in the Chiriveta section. Each interval shows a relative enrichment (up 10 to 30% compared to the
average value) in immobile elements such as Ti, Al and Zr (Fig. 5). To ensure that major and trace
concentrations are not grain-size biased, we plotted grain-size proxies Si/Al, Ti/Al and Zr/Al (Lupker et al.,
2012; Turner et al., 2015), which all exhibit a relatively stable trend, not correlated with the immobile element
concentrations (Figure S3 in the Supplement). The enrichments in Ti, Al and Zr suggest mature paleosols with
325 potential intense weathering due to enhanced humid climatic conditions; but may also correspond to a longer
exposure time on a stable floodplain, allowing leaching of mobile elements and relative enrichment of immobile
elements (Sheldon and Tabor, 2009). Pedogenic nodules are frequent in well-drained soil profiles associated
with a climate regime where the potential evapotranspiration is greater than the mean annual precipitation rate
(Slessarev et al., 2016) and with a mean annual precipitation < 800 mm/year (Cerling, 1984; Retallack, 1994;
330 Sheldon and Tabor, 2009). These conditions correspond to climate ranging from arid to sub-humid conditions
(Hasiotis, 2004; Hyland and Sheldon, 2013; Prochnow et al., 2006). This agrees with MAP values obtained for
the paleo-precipitation estimate (Fig. 5) and with a smectite/kaolinite >1 assemblage dominating some of the
studied soils (Nicolaidis, 2017, Table S1 in the Supplement); all fitting well with a semi-arid to sub-humid
contrasted climate with seasonal humidity (Arostegi et al., 2011). Associated with NCIEs C and D in red bed
335 deposits, sub-milimetric iron-oxide and hydroxides nodules made of concentric hematite and goethite were
found together with carbonate nodules. This suggest a contrasted climate as hematite forms under more arid soil
condition than goethite (Kraus and Riggins, 2007). Together, these observations are in line with an acceleration
of the hydrological cycle and a higher seasonality already observed during the PETM, H1, H2; I1 and I2
hyperthermals (Bowen et al., 2004; Dunkley Jones et al., 2018; Nicolo et al., 2007; Slotnick et al., 2012).
340 Therefore, combined with NCIEs, we suggest that small scale hyperthermals in continental records can be
recognized by an increase in the weathering index (Hessler et al., 2017) and by an increase in the immobile
element concentrations, both related to an increase in precipitation intensity.



5.3 High-resolution hyperthermal signal

The high-resolution isotopic and elemental record of the Chiriveta profile allow us to highlight the dynamics and variability of a hyperthermal event. We do not observe a unique peak in $\delta^{13}\text{C}$, but rather a stepped isotopic signal suggesting, together with above-discussed geochemical data, a climatic oscillation alternating with variably intense precipitations and leaching conditions during a climax spanning *ca.* 150 kyr (interval NCIE B to D). Such a climatic behaviour, already described during the pre-onset PETM excursion (Bowen et al., 2014), may indicate a back and forth climatic response to carbon cycle perturbations. Moreover, the $\delta^{13}\text{C}$ climax (NCIE D) does correspond neither to the highest concentrations of immobile elements nor maximum MAP estimates happening during NCIE C, since it predates from *ca.* 50 kyr the NCIE D (Fig. 7). The minimum $\delta^{13}\text{C}$ value therefore does not seem to be coeval with the most extreme climatic response, suggesting a complex environmental response. However, because sedimentation in floodplain depositional settings is a function of the channel position and flood frequency, the relative concentration of elements only likely reflects the changes in river dynamics instead of climatic variability, which could explain the mismatch between minimum values in NCIE and the climatic response. More high-resolution hyperthermal studies in coeval continental sections are needed to better understand the relationships between proxies.

5.4 Preservation potential of hyperthermals in continental sections

Since the first studies that applied sequence stratigraphy concepts onto continental deposits, the preservation of environmental signals in the continental stratigraphic record has been considered incomplete, especially during falling sea-level (Shanley and McCabe, 1994; Wright and Marriott, 1993). Even at higher-resolution timescales, floodplain deposits are still considered as fragmentary and discontinuous in nature due to non-continuous flood, avulsion, and channel migration sedimentation processes and the irregular depositional thickness relative to the position of the channel (Turner et al., 2015). This potential incompleteness of the sedimentary record (Barrell, 1917; Sadler, 1981) and the capacity of a sedimentary section to document a continuous paleoclimatic signal has probably led many workers to prefer the deep-marine records. Major events such as the PETM event has proven to be detectable in both marine and continental environments (e.g.; Abels et al., 2016; Koch et al., 1992), but the signal and preservation potential of smaller scale climatic events (e.g. hyperthermal events L to W in Lauretano et al., 2016), is somewhat uncertain (Foreman and Straub, 2017). Consequently, to assess in a quantitative matter the preservation potential of a hyperthermal event with a generic 40 kyr duration (Sexton et al., 2011), we calculated the compensation time scale (T_c). T_c is a characteristic time-scale in an alluvial basin below which stratigraphic signals with shorter durations may be of autogenic origin, thereby giving a scale below which allogenic forcing should be interpreted carefully (Foreman and Straub, 2017; Trampush et al., 2017; Wang et al., 2011). In other words, an external forcing signal with a duration smaller than T_c will be challenging to identify from background variability; the external forcing must be therefore of a longer duration than T_c and optimally twice T_c (Foreman and Straub, 2017). T_c max can be calculated by dividing the topographic roughness or maximum channel depth by the average subsidence or deposition rate (Wang et al., 2011). Based on preserved channel fills in La Roca and Chiriveta sections, we estimated a maximum channel depth to be 6 m with an average of 3.75 m (fitting previous measurements of maximum 7 m by Nijman and Puigdefabregas (1978)). With a thickness of 150 m for the Castissent Fm in the La Roca section (Marzo et al., 1988) and of 101 m in the Chiriveta section (this study) and using the maximum and minimum age extension of



the Formation, we obtain sedimentation rates between 0.1 and 0.29 mm/yr. These values are within sedimentation rates of Eocene floodplain succession (Kraus and Aslan, 1993). Using an average sedimentation rate of 0.17 m/kyr, we obtained a mean T_c of 22,000 yrs. A hyperthermal event of 40 kyr, being approximately
385 twice as long as the estimated T_c , should be recorded.

There are five Eocene hyperthermal events (PETM, ETM2/ELMO/H1, H2, I1, I2) identified worldwide (e.g.; Abels et al., 2016; Schmitz and Pujalte, 2003). If we add the data from this study (U event), we can estimate a mean thickness for hyperthermal events of *ca.* 27 m for continental and 1.3 m for deep-marine succession, respectively (Abels et al., 2016; Bowen et al., 2001; Laurentano et al., 2015; Lourens et al., 2005; Nicolo et al.,
390 2007; Schmitz and Pujalte, 2003; Slotnick et al., 2012; Westerhold et al., 2018). Thus, regarding the hitherto studied sections, terrestrial strata recording hyperthermals are potentially one order of magnitude thicker with resolutions likely higher than deep-marine sections. Therefore, continental strata, which are directly linked to environmental conditions occurring at the time of their formation, might preserve a better record of past climatic events (Sheldon and Tabor, 2009). The continental record of past climatic events might have been overlooked; if
395 such record can be proved complete, the potential climatic events preservation is higher and likely of high resolution.

6 Conclusions

A new high-resolution isotopic record from the paleosol-rich Chiriveta section succession allows to identify a prominent negative carbon isotope excursion (NCIE) in continental deposits that we suggest to be the “U” event,
400 providing new insights into the climate and carbon cycle dynamics during a hyperthermal event. This climatic event, identified for the first time in continental deposits, reaches $\delta^{13}\text{C}$ values of 2 sigma (standard deviation) below the mean and is preceded and followed by several smaller-scale stepped NCIEs, which are interpreted as moments of enhanced primary productivity, leading to an overall higher soil respiration. We show that all these NCIEs are relatively enriched in immobile elements (i.e., Ti, Zr and Al) and display an increase in MAP
405 estimates. These observations coupled with the presence of iron-oxide nodules on an overall weathered succession, suggest a contrasted climate and an increase in precipitation rates during these events. The data presented in this study suggests a period of *ca.* 150 kyr of oscillating climate alternating average and above background weathering conditions. Finally, the results of this study provide support to the recognition and importance of hyperthermal events in continental successions as well as in the preservation potential of such
410 deposits.

Acknowledgements. The authors would like to acknowledge the lifetime work of Josep Serra Kiel, whose research and scientific contributions in the Pyrenees have been fundamental to this work and much beyond. This study has benefited from scientific discussion and field work with M. Perret, A. Nowak, C. Lauchli, T. Hunger,
415 J. Vernier and T. Maeder. Work supported by an Augustin Lombard grant from the SPHN Society of Geneva. Field work was supported by an Equinor grant to SC.

Isotopic, majors and trace data can be found in the supporting information (Table S2 in the Supplement)



420 **Author contributions.** LH led the field work, sampling, sample preparation, data interpretation and writing. TA
contributed to field work, sampling, data interpretation, discussion and writing. JES performed stable isotope
analysis, data interpretation and writing. JKR interpreted the data and writing. MPM and EC contributed to
fieldwork, sampling, discussion and writing. CP, JC and AF supervised the fieldwork, discussions and writing.
EV led discussions on the paleosols. KK and MH performed the XRF analysis. SC supervised the project and
425 writing.

The authors declare that they have no conflict of interest

References

- Abels, H. a., Clyde, W. C., Gingerich, P. D., Hilgen, F. J., Fricke, H. C., Bowen, G. J. and Lourens, L. J.:
430 Terrestrial carbon isotope excursions and biotic change during Palaeogene hyperthermals, *Nat. Geosci.*, 5, 326–
329, doi:10.1038/ngeo1427, 2012.
- Abels, H. A., Lauretano, V., van Yperen, A. E., Hopman, T., Zachos, J. C., Lourens, L. J., Gingerich, P. D. and
Bowen, G. J.: Environmental impact and magnitude of paleosol carbonate carbon isotope excursions marking
five early Eocene hyperthermals in the Bighorn Basin, Wyoming, *Clim. Past*, 12, 1151–1163, doi:10.5194/cp-
435 12-1151-2016, 2016.
- Arostegi, J., Baceta, J. I., Pujalte, V. and Carracedo, M.: Late Cretaceous – Palaeocene mid-latitude climates:
inferences from clay mineralogy of continental-coastal sequences (Trempe-Graus area, southern Pyrenees, N
Spain), *Clay Miner.*, 46, 105–126, doi:10.1180/claymin.2011.046.1.105, 2011.
- Barrell, J.: Rhythms and measurement of geologic time, *Geol. Soc. Am. Bull.*, 28, 745–904, 1917.
- 440 Bentham, P. and Burbank, D. W.: Chronology of Eocene foreland basin evolution along the western oblique
margin of the South-Central Pyrenees., *Tert. Basins Spain. Stratigr. Rec. Crustal Kinematics. World Reg. Geol.*,
6, 144–152, 1996.
- Bolle, M. P. and Adatte, T.: Palaeocene early Eocene climatic evolution in the Tethyan realm: clay mineral
evidence, *Clay Miner.*, 36, 249–261, doi:10.1180/000985501750177979, 2001.
- 445 Bowen, G. J., Koch, P. L., Gingerich, P. D., Norris, R. D., Bains, S. and Corfield, R. M.: Refined isotope
stratigraphy across the continental Paleocene-Eocene boundary on Polecat Bench in the northern Bighorn Basin,
Int. Conf. Clim. biota early Paleogene, Powell, WY, United States, July 3-8, 2001, 33, 73–88, 2001.
- Bowen, G. J., Beerling, D. J., Koch, P. L., Zachos, J. C. and Quattlebaum, T.: A humid climate state during the
Palaeocene / Eocene thermal maximum, *Nature*, 432, 495–499, doi:10.1038/nature03109.1., 2004.
- 450 Bowen, G. J., Bralower, T. J., Delaney, M. L., Dickens, G. R., Kelly, D. C., Koch, P. L., Kump, L. R., Meng, J.,
Sloan, L. C., Thomas, E., Wing, S. L. and Zachos, J. C.: Eocene hyperthermal event offers insight into
greenhouse warming, *Eos, Trans. Am. Geophys. Union*, 87, 165, doi:10.1029/2006EO170002, 2006.
- Bowen, G. J., Maibauer, B. J., Kraus, M. J., Röhl, U., Westerhold, T., Steimke, A., Gingerich, P. D., Wing, S. L.
and Clyde, W. C.: Two massive, rapid releases of carbon during the onset of the Palaeocene-Eocene thermal
455 maximum, *Nat. Geosci.*, 8, 44–47, doi:10.1038/ngeo2316, 2014.
- Bull, W. B.: *Geomorphic Responses to Climate Change*. Oxford University Press, New York, 1991.
- Carmichael, M. J., Inglis, G. N., Badger, M. P. S., Naafs, B. D. A., Behrooz, L., Rimmelzwaal, S., Monteiro, F.
M., Rohrsen, M., Farnsworth, A., Buss, H. L., Dickson, A. J., Valdes, P. J., Lunt, D. J. and Pancost, R. D.:



- Hydrological and associated biogeochemical consequences of rapid global warming during the Paleocene-
460 Eocene Thermal Maximum, *Glob. Planet. Change*, 157, 114–138, doi:10.1016/j.gloplacha.2017.07.014, 2017.
- Carrillo, Y., Dijkstra, F., LeCain, D., Blumenthal, D. and Pendall, E.: Elevated CO₂ and warming cause interactive effects on soil carbon and shifts in carbon use by bacteria, *Ecol. Lett.*, doi:10.1111/ele.13140, 2018.
- Castellort, S. and Van Den Driessche, J.: How plausible are high-frequency sediment supply-driven cycles in the stratigraphic record?, *Sediment. Geol.*, 157, 3–13, doi:10.1016/S0037-0738(03)00066-6, 2003.
- 465 Castellort, S., Honegger, L., Adatte, T., Clark, J. D., Puigdefàbregas, C., Spangenberg, J. E., Dykstra, M. L. and Fildani, A.: Detecting eustatic and tectonic signals with carbon isotopes in deep-marine strata, Eocene Ainsa Basin, Spanish Pyrenees, *Geology*, 45, 707–710, doi:10.1130/G39068.1, 2017.
- Cerling, T. E.: The stable isotopic composition of modern soil carbonate and its relation to climate, *Earth Planet. Sci. Lett.*, 71, 229–240., 1984.
- 470 Cerling, T. E. and Quade, J.: Stable Carbon and Oxygen Isotopes in Soil Carbonates, *Clim. Chang. Cont. Isot. Rec.*, 217–231, doi:10.1029/GM078p0217, 1993.
- Chanvry, E., Deschamps, R., Joseph, P., Puigdefàbregas, C., Poyatos-Moré, M., Kiel, J. S., Garcia, D. and Teinturier, S.: The influence of intrabasinal tectonics in the stratigraphic evolution of piggyback basin fills: Towards a model from the Tremp–Graus–Ainsa Basin (South-Pyrenean Zone, Spain), *Sediment. Geol.*, 377, 34–
475 62, doi:10.1016/j.sedgeo.2018.09.007, 2018.
- Checa-Soler, L.: Revisión del género *Diacodexis* (Artiodactyla, Mammalia) en el Eoceno inferior del Noreste de España, *Geobios*, 37, 325–335, doi:10.1016/j.geobios.2004.03.001, 2004.
- Chen, C., Guerit, L., Foreman, B. Z., Hassenruck-Gudipati, H. J., Adatte, T., Honegger, L., Perret, M., Sluijs, A. and Castellort, S.: Estimating regional flood discharge during Palaeocene-Eocene global warming, *Sci. Rep.*, 8,
480 1–8, doi:10.1038/s41598-018-31076-3, 2018.
- Cramer, B. S., Wright, J. D., Kent, D. V. and Aubry, M. P.: Orbital climate forcing of $\delta^{13}\text{C}$ excursions in the late Paleocene-early Eocene (chrons C24n–C25n), *Paleoceanography*, 18, 1–25, doi:10.1029/2003PA000909, 2003.
- Croudace, I. W. and Rothwell, R. G.: *Micro-XRF Studies of Sediment Cores: Applications of a non-destructive*
485 *Tool for the Environmental Sciences*, edited by I. W. Croudace and R. G. Rothwell, Springer Netherlands, Dordrecht., 2015.
- Davidson, E. A. and Janssens, I. A.: Temperature sensitivity of soil carbon decomposition and feedbacks to climate change, *Nature*, 440, 165–173, doi:10.1038/nature04514, 2006.
- Davidson, E. A., Trumbore, S. E. and Amundson, R.: Soil warming and organic carbon content, *Nature*, 408,
490 789–790, 2000.
- Deconto, R. M., Galeotti, S., Pagani, M., Tracy, D., Schaefer, K., Zhang, T., Pollard, D. and Beerling, D. J.: Past extreme warming events linked to massive carbon release from thawing permafrost, *Nature*, 484, 87–91, doi:10.1038/nature10929, 2012.
- Doetterl, S., Stevens, A., Six, J., Merckx, R., Van Oost, K., Casanova Pinto, M., Casanova-Katny, A., Muñoz,
495 C., Boudin, M., Zagal Venegas, E. and Boeckx, P.: Soil carbon storage controlled by interactions between geochemistry and climate, *Nat. Geosci.*, 8, 780–783, doi:10.1038/ngeo2516, 2015.



- Duller, R. A., Armitage, J. J., Manners, H. R., Grimes, S. and Jones, T. D.: Delayed sedimentary response to abrupt climate change at the Paleocene-Eocene boundary, northern Spain, *Geology*, 47, 159–162, doi:10.1130/G45631.1, 2019.
- 500 Dunkley Jones, T., Manners, H. R., Hoggett, M., Turner, S. K., Westerhold, T., Leng, M. J., Pancost, R. D., Ridgwell, A., Alegret, L., Duller, R. and Grimes, S. T.: Dynamics of sediment flux to a bathyal continental margin section through the Paleocene-Eocene Thermal Maximum, *Clim. Past*, 14, 1035–1049, doi:10.5194/cp-14-1035-2018, 2018.
- Foreman, B. Z. and Straub, K. M.: Autogenic geomorphic processes determine the resolution and fidelity of
505 terrestrial paleoclimate records, *Sci. Adv.*, 3, 1–12, doi:10.1126/sciadv.1700683, 2017.
- Foreman, B. Z., Heller, P. L. and Clementz, M. T.: Fluvial response to abrupt global warming at the Palaeocene/Eocene boundary, *Nature*, 490, 92–95, doi:10.1038/nature11513, 2012.
- Gallagher, T. M. and Sheldon, N. D.: Combining soil water balance and clumped isotopes to understand the nature and timing of pedogenic carbonate formation, *Chem. Geol.*, doi:10.1016/j.chemgeo.2016.04.023, 2016.
- 510 Hasiotis, S. T.: Reconnaissance of Upper Jurassic Morrison Formation ichnofossils, Rocky Mountain Region, USA: Paleoenvironmental, stratigraphic, and paleoclimatic significance of terrestrial and freshwater ichnoecoenoses, *Sediment. Geol.*, 167, 177–268, doi:10.1016/j.sedgeo.2004.01.006, 2004.
- Hessler, A. M., Zhang, J., Covault, J. and Ambrose, W.: Continental weathering coupled to Paleogene climate changes in North America, *Geology*, 45, doi:10.1130/G39245.1, 2017.
- 515 Hunger, T.: Climatic signals in the Paleocene fluvial formation of the Tresp-Graus Basin, Pyrenees, Spain., University of Geneva., 2018.
- Hyland, E. G. and Sheldon, N. D.: Coupled CO₂-climate response during the Early Eocene Climatic Optimum, *Palaeogeogr. Palaeoclimatol. Palaeoecol.*, 369, 125–135, doi:10.1016/j.palaeo.2012.10.011, 2013.
- Kapellos, C. and Schaub, H.: Zur Korrelation von Biozonierungen mit Grossforaminiferen und Nannoplankton
520 im Paläogen der Pyrenäen, *Eclogae Geol. Helv.*, 66, 687–737, 1973.
- Khozyem Saleh, H. M. A.: Sedimentology, geochemistry and mineralogy of the Paleocene-Eocene Thermal Maximum (PETM): sediment records from Egypt, India and Spain Hassan Mohamed Ahmed Khozyem SALEH; 2013, Université de Lausanne., 2013.
- Klemmedson, J. O.: Soil organic matter in arid and semiarid ecosystems: Sources, accumulation, and
525 distribution, *Arid Soil Res. Rehabil.*, 3, 99–114, doi:10.1080/15324988909381194, 1989.
- Koch, P. L., Zachos, J. C. and Gingerich, P. D.: Correlation between isotope records in marine and continental carbon reservoirs near the Palaeocene/Eocene boundary, *Nature*, 358, 319–322, doi:10.1038/358319a0, 1992.
- Koch, P. L., Zachos, J. and Dettman, D. L.: Stable isotope stratigraphy and paleoclimatology of the Paleogene Bighorn Basin (Wyoming, USA), *Palaeogeogr. Palaeoclimatol. Palaeoecol.*, 115, 61–89, doi:10.1016/0031-
530 0182(94)00107-J, 1995.
- Koch, P. L., Clyde, W. C., Hepple, R. P., Fogel, M. L., Wing, S. L. and Zachos, J. C.: Carbon and oxygen isotope records from Paleosols spanning the Paleocene-Eocene boundary, Bighorn Basin, Wyoming, Causes Consequences *Glob. Warm Clim. Early Paleogene*, 369, 49–64, doi:https://doi.org/10.1130/0-8137-2369-8.49, 2003.
- 535 Koven, C. D., Hugelius, G., Lawrence, D. M. and Wieder, W. R.: Higher climatological temperature sensitivity of soil carbon in cold than warm climates, *Nat. Clim. Chang.*, 7, 817–822, doi:10.1038/nclimate3421, 2017.



- Kraus, M. J. and Aslan, A.: Eocene hydromorphic paleosols: significance for interpreting ancient floodplain processes, *J. Sediment. Res.*, 63, 453–463, doi:10.1306/D4267B22-2B26-11D7-8648000102C1865D, 1993.
- Kraus, M. J. and Riggins, S.: Transient drying during the Paleocene-Eocene Thermal Maximum (PETM):
540 Analysis of paleosols in the bighorn basin, Wyoming, *Palaeogeogr. Palaeoclimatol. Palaeoecol.*, 245, 444–461, doi:10.1016/j.palaeo.2006.09.011, 2007.
- Lauretano, V., Littler, K., Polling, M., Zachos, J. C. and Lourens, L. J.: Frequency, magnitude and character of hyperthermal events at the onset of the Early Eocene Climatic Optimum, *Clim. Past*, 11, 1313–1324, doi:10.5194/cp-11-1313-2015, 2015.
- 545 Lauretano, V., Hilgen, F. J., Zachos, J. C. and Lourens, L. J.: Astronomically tuned age model for the early Eocene carbon isotope events: A new high-resolution $\delta^{13}\text{C}$ benthic record of ODP Site 1263 between ~49 and ~54 Ma, *Earth Planet. Sci. Lett.*, 49, 383–400, doi:10.1016/j.epsl.2016.07.007, 2016.
- Lourens, L. J., Sluijs, A., Kroon, D., Zachos, J. C., Thomas, E., Röhl, U., Bowles, J. and Raffi, I.: Astronomical pacing of late Palaeocene to early Eocene global warming events, *Nature*, 435, 1083–1087,
550 doi:10.1038/nature03814, 2005.
- Lunt, D. J., Ridgwell, A., Sluijs, A., Zachos, J., Hunter, S. and Haywood, A.: A model for orbital pacing of methane hydrate destabilization during the Palaeogene, *Nat. Geosci.*, 4, 775–778, doi:10.1038/ngeo1266, 2011.
- Lupker, M., France-Lanord, C., Lavé, J., Bouchez, J., Galy, V., Métivier, F., Gaillardet, J., Lartiges, B. and Mugnier, J.-L.: A Rouse-based method to integrate the chemical composition of river sediments: Application to
555 the Ganga basin, *J. Geophys. Res.*, 116, F04012, doi:10.1029/2010JF001947, 2011.
- Lupker, M., France-Lanord, C., Galy, V., Lavé, J., Gaillardet, J., Gajurel, A. P., Guilmette, C., Rahman, M., Singh, S. K. and Sinha, R.: Predominant floodplain over mountain weathering of Himalayan sediments (Ganga basin), *Geochim. Cosmochim. Acta*, 84, 410–432, doi:10.1016/j.gca.2012.02.001, 2012.
- Marzo, M., Nijman, W. and Puigdefabregas, C.: Architecture of the Castissent fluvial sheet sandstones, Eocene,
560 South Pyrenees, Spain, *Sedimentology*, 35, 719–738, doi:10.1111/j.1365-3091.1988.tb01247.x, 1988.
- McInerney, F. A. and Wing, S. L.: The Paleocene-Eocene Thermal Maximum: A Perturbation of Carbon Cycle, Climate, and Biosphere with Implications for the Future, *Annu. Rev. Earth Planet. Sci.*, 39, 489–516, doi:10.1146/annurev-earth-040610-133431, 2011.
- Melillo, J. M., Stuedler, P. A., Aber, J. D. M., Newkirk, K., Lux, H., Bowles, F. P., Catricala, C., Magill, A.,
565 Ahrens, T. and Morrisseau, S.: Soil warming and carbon-cycle feedbacks to the climate system, *Science* (80-.), 323, 2173–2176, doi:10.1126/science.1258433, 2014.
- Millière, L., Spangenberg, J. E., Bindschedler, S., Cailleau, G. and Verrecchia, E. P.: Reliability of stable carbon and oxygen isotope compositions of pedogenic needle fibre calcite as environmental indicators: Examples from Western Europe, *Isotopes Environ. Health Stud.*, 47, 341–358,
570 doi:10.1080/10256016.2011.601305, 2011a.
- Millière, L., Hasinger, O., Bindschedler, S., Cailleau, G., Spangenberg, J. E. and Verrecchia, E. P.: Stable carbon and oxygen isotope signatures of pedogenic needle fibre calcite, *Geoderma*, 161, 74–87, doi:10.1016/j.geoderma.2010.12.009, 2011b.
- Mutti, E., Séguret, M. and Sgavetti, M.: Sedimentation and Deformation in the Tertiary Sequences of the
575 Southern Pyrenees., 1988.



- Nicolaides, E.: Analyses des sédiments marins et continentaux éocènes dans les Pyrénées Espagnoles, Université de Lausanne., 2017.
- Nicolo, M. J., Dickens, G. R., Hollis, C. J. and Zachos, J. C.: Multiple early Eocene hyperthermals: Their sedimentary expression on the New Zealand continental margin and in the deep sea, *Geology*, 35, 699, doi:10.1130/G23648A.1, 2007.
- 580 Nijman, W.: Cyclicity and basin axis shift in a piggyback basin: towards modelling of the Eocene Tresp-Ager Basin, South Pyrenees, Spain, *Geol. Soc. London, Spec. Publ.*, 134, 135–162, doi:10.1144/GSL.SP.1998.134.01.07, 1998.
- Nijman, W. and Nio, S.-D.: The Eocene Montañana Delta, 1975.
- 585 Nijman, W. and Puigdefabregas, C.: Coarse-grained point bar structure in a molasse-type fluvial system, Eocene Castissent sandstone Formation, south Pyrenean Basin., *Fluv. Sedimentol. Can Soc Pet. Geol Mem* 5, 5, 487–510, 1978.
- Paillard, D., Labeyrie, L. and Yiou, P.: Macintosh Program performs time-series analysis, *Eos, Trans. Am. Geophys. Union*, doi:10.1029/96EO00259, 1996.
- 590 Payros, A. and Tosquella, J.: Filling the North European Early/Middle Eocene (Ypresian/Lutetian) boundary gap: insights from the Pyrenean continental to deep-marine record, *Palaeogeogr. Palaeoclimatol. Palaeoecol.*, 280, 313–332, doi:10.1016/j.palaeo.2009.06.018, 2009.
- Payros, A., Ortiz, S., Millán, I., Arostegi, J., Orue-Etxebarria, X. and Apellaniz, E.: Early Eocene climatic optimum: Environmental impact on the North Iberian continental margin, *Bull. Geol. Soc. Am.*, 127, 1632–1644, doi:10.1130/B31278.1, 2015.
- 595 Pickering, K. T. and Bayliss, N. J.: Deconvolving tectono-climatic signals in deep-marine siliciclastics, Eocene Ainsa basin, Spanish Pyrenees: Seesaw tectonics versus eustasy, *Geology*, 37, 203–206, doi:10.1130/G25261A.1, 2009.
- Poyatos-Moré, M.: Physical Stratigraphy and Facies Analysis of the Castissent Tecto-Sedimentary Unit., 2014.
- 600 Prochnow, S. J., Nordt, L. C., Atchley, S. C. and Hudec, M. R.: Multi-proxy paleosol evidence for middle and late Triassic climate trends in eastern Utah, *Palaeogeogr. Palaeoclimatol. Palaeoecol.*, 232, 53–72, doi:10.1016/j.palaeo.2005.08.011, 2006.
- Puigdefabregas, C., Souquet, P., Puigdefabregas, C. and Souquet, P.: Tecto-sedimentary cycles and depositional sequences of the mesozoic and tertiary from the pyrenees, *Tectonophysics*, 129, 173–203, doi:10.1016/0040-1951(86)90251-9, 1986.
- 605 Pujalte, V., Baceta, J. I. and Schmitz, B.: A massive input of coarse-grained siliciclastics in the Pyrenean Basin during the PETM: The missing ingredient in a coeval abrupt change in hydrological regime, *Clim. Past*, 11, 1653–1672, doi:10.5194/cp-11-1653-2015, 2015.
- Raich, J. and Schlesinger, W.: The global carbon dioxide flux in soil respiration, *Tellus*, 44 B, 81–99, 1992.
- 610 Retallack, G. J.: The Environmental Factor Approach to the Interpretation of Paleosols, *Factors Soil Form. A Fiftieth Anniv. Retrospect., SSSA Speci.*, 31–63, 1994.
- Romans, B. W., Castellort, S., Covault, J. A., Fildani, A. and Walsh, J. P. P.: Environmental signal propagation in sedimentary systems across timescales, *Earth-Science Rev.*, 153, 7–29, doi:10.1016/j.earscirev.2015.07.012, 2016.



- 615 Sadler, P. M.: Sediment Accumulation Rates and the Completeness of Stratigraphic Sections, *J. Geol.*, 89, 569–584, doi:10.1086/628623, 1981.
- Schaub, H.: Über die Grossforaminiferen im Untereocaen von Campo (Ober-Aragonien), *Eclogae Geol. Helv.*, 59, 355–391, 1966.
- Schaub, H.: Nummulites et Assilines de la Téthys paléogène: Taxionomie, phylogénèse et biostratigraphie, *Mém. suisse Paléont.*, 104, 236 p., 1981.
- 620 Schimel, D. S., Braswell, B. H., Holland, E. A., Mckeown, R., Ojima, D. S., Painter, H., Parton, W. J. and Townsend, A. R.: Climatic, edaphic, and biotic controls over storage and turnover of carbon in soils, *Global Biogeochem. Cycles*, 8, 279–293, 1994.
- Schlunegger, F. and Castellort, S.: Immediate and delayed signal of slab breakoff in Oligo/Miocene Molasse deposits from the European Alps, *Sci. Rep.*, 6, doi:10.1038/srep31010, 2016.
- 625 Schmitz, B. and Pujalte, V.: Sea-level, humidity, and land-erosion records across the initial Eocene thermal maximum from a continental-marine transect in northern Spain, *Geology*, 31, 689–692, doi:10.1130/G19527.1, 2003.
- Sexton, P. F., Norris, R. D., Wilson, P. A., Pälike, H., Westerhold, T., Röhl, U., Bolton, C. T. and Gibbs, S.: Eocene global warming events driven by ventilation of oceanic dissolved organic carbon, *Nature*, 471, 349–353, doi:10.1038/nature09826, 2011.
- 630 Shanley, K. and McCabe, P.: Perspectives on the sequence stratigraphy of continental strata, *Am. Assoc. Pet. Geol. Bull.*, 4, 544–568, 1994.
- Sheldon, N. D. and Tabor, N. J.: Quantitative paleoenvironmental and paleoclimatic reconstruction using paleosols, *Earth-Science Rev.*, 95, 1–52, doi:10.1016/j.earscirev.2009.03.004, 2009.
- 635 Sheldon, N. D., Retallack, G. J. and Tanaka, S.: Geochemical Climofunctions from North American Soils and Application to Paleosols across the Eocene-Oligocene Boundary in Oregon, *J. Geol.*, 110, 687–696, doi:10.1086/342865, 2002.
- Slessarev, E. W., Lin, Y., Bingham, N. L., Johnson, J. E., Dai, Y., Schimel, J. P. and Chadwick, O. A.: Water balance creates a threshold in soil pH at the global scale, *Nature*, 540, 567–569, doi:10.1038/nature20139, 2016.
- 640 Slotnick, B. S., Dickens, G. R., Nicolo, M. J., Hollis, C. J., Crampton, J. S., Zachos, J. C. and Sluijs, A.: Large-Amplitude Variations in Carbon Cycling and Terrestrial Weathering during the Latest Paleocene and Earliest Eocene: The Record at Mead Stream, New Zealand, *J. Geol.*, 120, 487–505, doi:10.1086/666743, 2012.
- Sluijs, A. and Dickens, G. R.: Assessing offsets between the $\delta^{13}\text{C}$ of sedimentary components and the global exogenic carbon pool across early Paleogene carbon cycle perturbations, *Global Biogeochem. Cycles*, 26, 1–14, doi:10.1029/2011GB004224, 2012.
- 645 Stap, L., Lourens, L. J., Thomas, E., Sluijs, A., Bohaty, S. and Zachos, J. C.: High-resolution deep-sea carbon and oxygen isotope records of Eocene Thermal Maximum 2 and H2, *Geology*, 38, 607–610, doi:10.1130/G30777.1, 2010.
- 650 Straub, K. M. and Foreman, B. Z.: Geomorphic stasis and spatiotemporal scales of stratigraphic completeness, *Geology*, 46, 311–314, doi:10.1130/G40045.1, 2018.
- Teixell, A.: Crustal structure and orogenic material budget in the west central Pyrenees, *Tectonics*, 17, 395–406, doi:10.1029/98TC00561, 1998.



- Torn, M. S., Trumbore, S. E., Chadwick, O. A., Vitousek, P. M. and Hendricks, D. M.: Mineral control of soil
655 organic carbon storage and turnover, *Nature*, 389, 170–173, doi:10.1038/38260, 1997.
- Tosquella, J.: Els Nummulitinae del Paleocè-Eocè inferior de la conca sudpirinenca, Universitat de Barcelona.,
1995.
- Trampush, S. M., Hajek, E. A., Straub, K. M. and Chamberlin, E. P.: Identifying autogenic sedimentation in
fluvial-deltaic stratigraphy: Evaluating the effect of outcrop-quality data on the compensation statistic, *J.*
660 *Geophys. Res. Earth Surf.*, 122, 91–113, doi:10.1002/2016JF004067, 2017.
- Trumbore, S., Chadwick, O. and Amundson, R.: Rapid exchange between soil carbon and atmospheric carbon
dioxide driven by temperature change, *Science* (80-.), 272, 393–396, 2006.
- Turner, J. N., Jones, A. F., Rassner, S. M., Macklin, M. G. and Brewer, P. A.: Micro-XRF Applications in
Fluvial Sedimentary Environments of Britain and Ireland: Progress and Prospects, in *In Micro-XRF Studies of*
665 *Sediment Cores*, pp. 227–265, Springer, Dordrecht., 2015.
- Turner, S. K., Sexton, P. F., Charles, C. D. and Norris, R. D.: Persistence of carbon release events through the
peak of early Eocene global warmth, *Nat. Geosci.*, 7, 748–751, doi:10.1038/NGEO2240, 2014.
- Wang, Y., Straub, K. M. and Hajek, E. a.: Scale-dependent compensational stacking: An estimate of autogenic
time scales in channelized sedimentary deposits, *Geology*, 39, 811–814, doi:10.1130/G32068.1, 2011.
- 670 Westerhold, T. and Röhl, U.: High resolution cyclostratigraphy of the early Eocene - New insights into the origin
of the Cenozoic cooling trend, *Clim. Past*, 5, 309–327, doi:10.5194/cp-5-309-2009, 2009.
- Westerhold, T., Röhl, U., Frederichs, T., Agnini, C., Raffi, I., Zachos, J. C. and Wilkens, R. H.: Astronomical
calibration of the Ypresian timescale: Implications for seafloor spreading rates and the chaotic behavior of the
solar system?, *Clim. Past*, 13, 1129–1152, doi:10.5194/cp-13-1129-2017, 2017.
- 675 Westerhold, T., Röhl, U., Donner, B. and Zachos, J. C.: Global Extent of Early Eocene Hyperthermal Events: A
New Pacific Benthic Foraminiferal Isotope Record From Shatsky Rise (ODP Site 1209), *Paleoceanogr.*
Paleoclimatology, 33, 626–642, doi:10.1029/2017PA003306, 2018.
- Whitchurch, a. L., Carter, A., Sinclair, H. D., Duller, R. a., Whittaker, a. C. and Allen, P. a.: Sediment routing
system evolution within a diachronously uplifting orogen: Insights from detrital zircon thermochronological
680 analyses from the South-Central Pyrenees, *Am. J. Sci.*, 311, 442–482, doi:10.2475/05.2011.03, 2011.
- Wright, V. P. and Marriott, S. B.: The sequence stratigraphy of fluvial depositional systems: the role of
floodplain sediment storage, *Sediment. Geol.*, 86, 203–210, doi:10.1016/0037-0738(93)90022-W, 1993.
- Zachos, J., Pagani, H., Sloan, L., Thomas, E. and Billups, K.: Trends, rhythms, and aberrations in global climate
65 Ma to present, *Science*, 292, 686–693, doi:10.1126/science.1059412, 2001.
- 685 Zachos, J., Dickens, G. and Zeebe, R.: An early Cenozoic perspective on greenhouse warming and carbon-cycle
dynamics., *Nature*, 451, 279–83, doi:10.1038/nature06588, 2008.



690

695

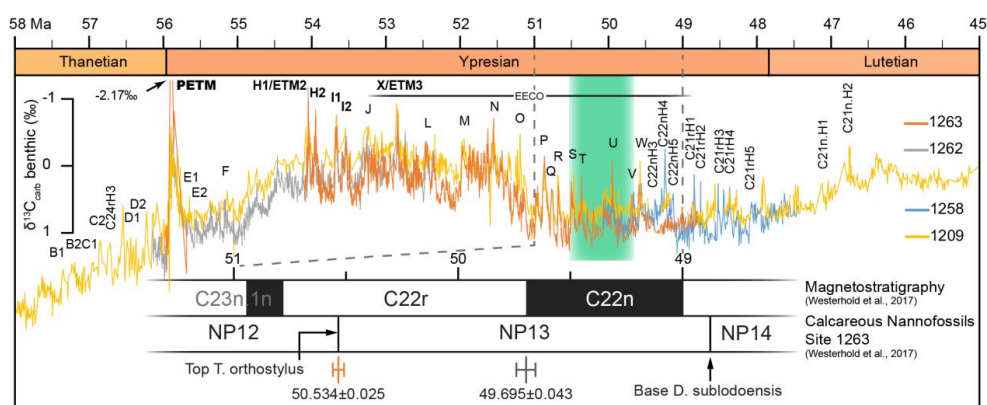
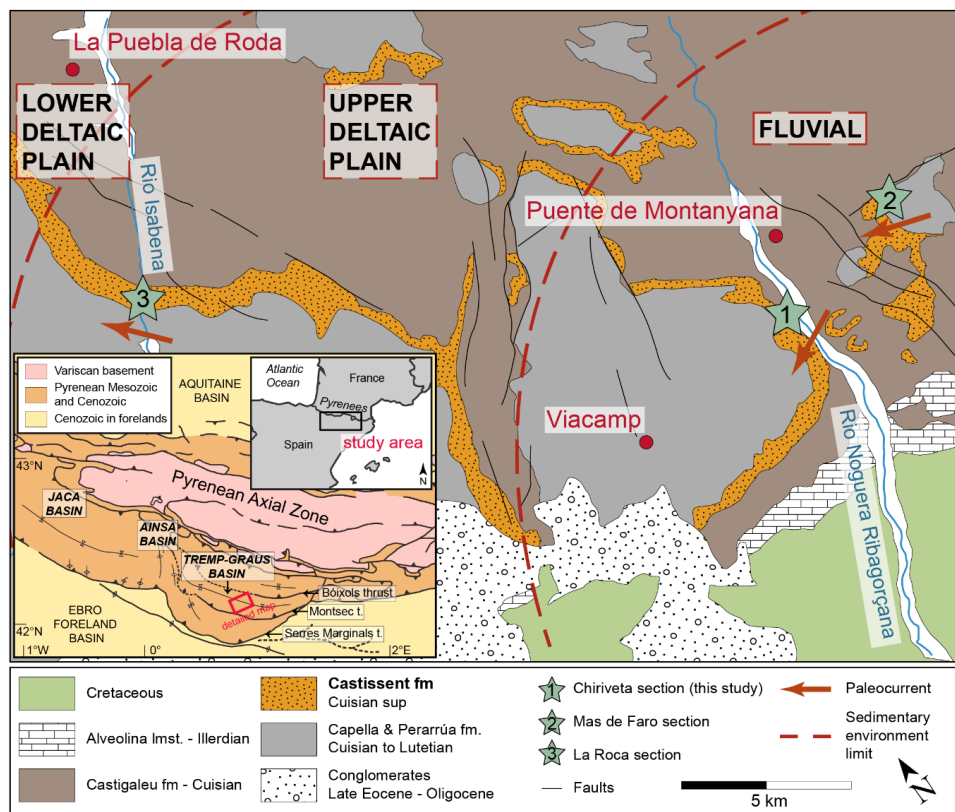
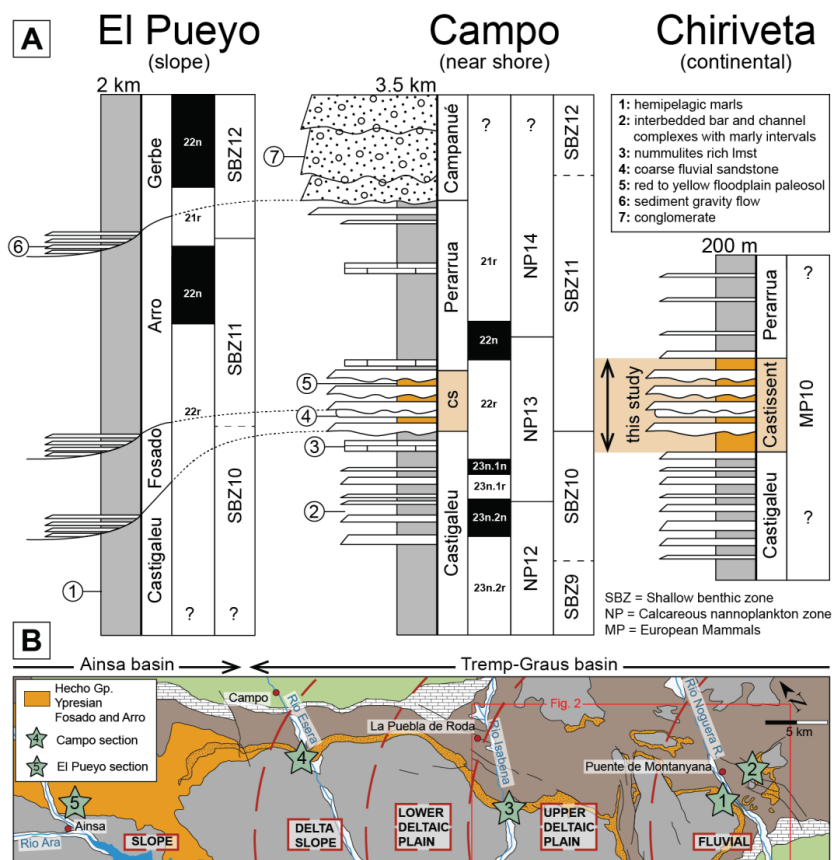


Figure 1: Late Paleocene and early-Eocene benthic carbon isotope record from Sites 1209, 1258, 1262 and 1263. Top of Chron C22r and top of *T. orthostylus* zone from site 1263 from Westerhold et al. (2017). Hyperthermal nomenclature from Laurentano et al. (2016) and Westerhold et al. (2017). Castissent Fm extension in green.

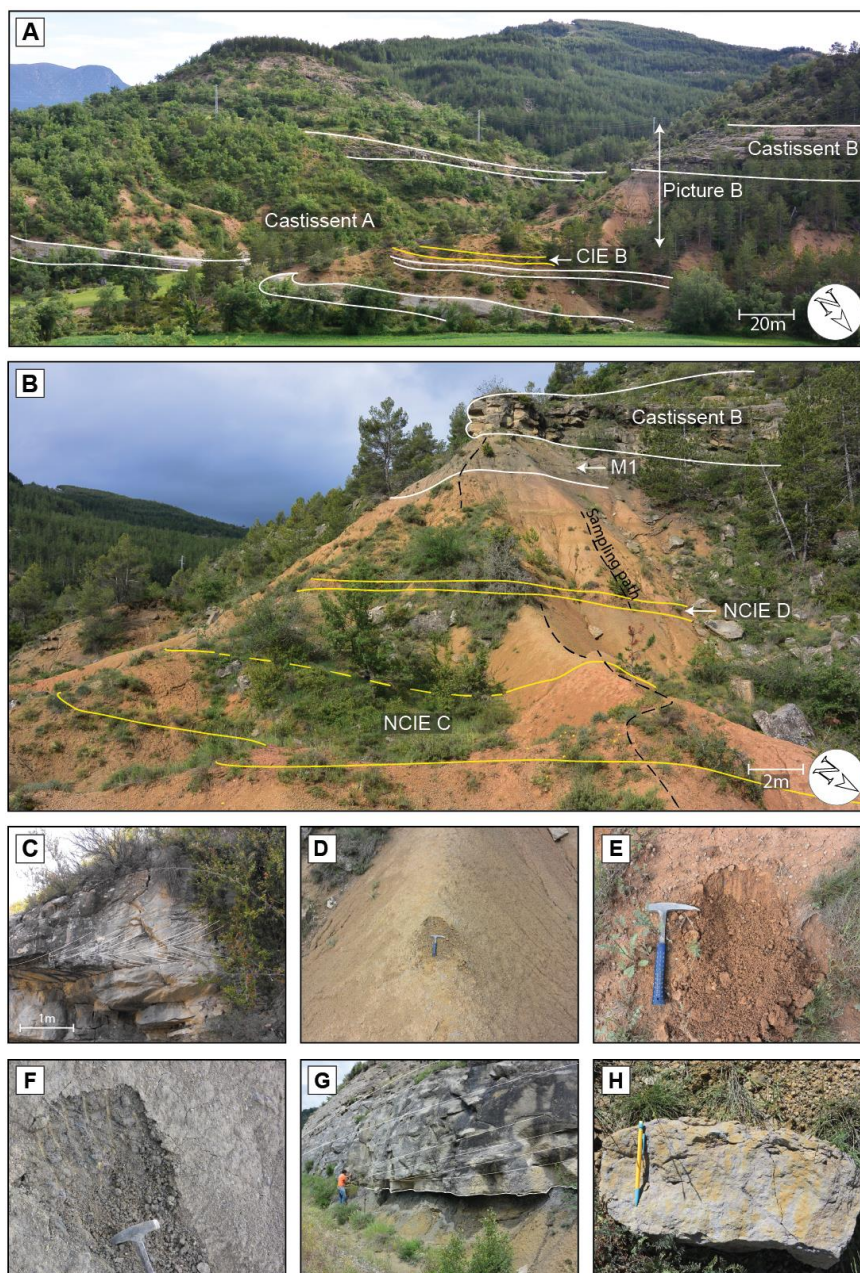
700



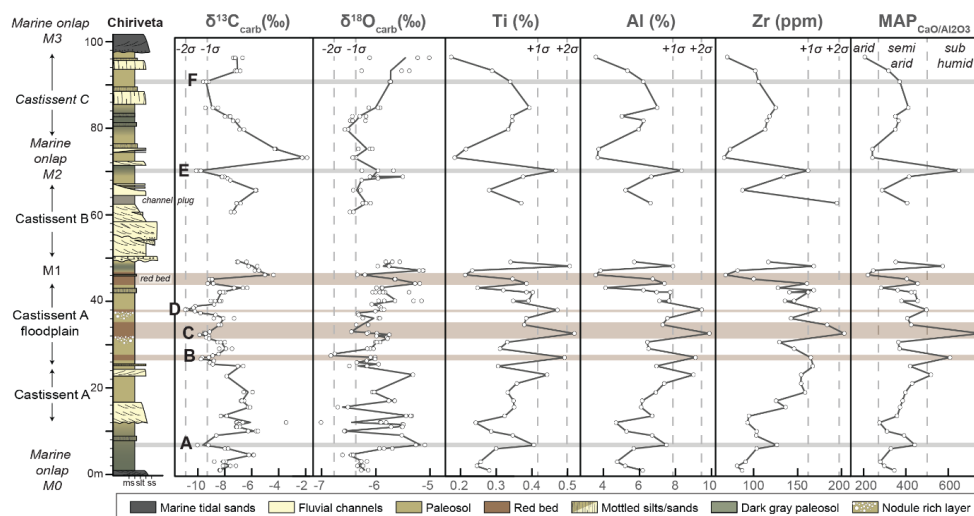
705 **Figure 2: Simplified situation and geological map of the study area with main depositional paleo-environments (e.g., Nijman, 1998). The Castissent Fm is a prominent fluvial unit particularly well-exposed in the Noguera Ribagorçana and Isabena river valleys. (1) Chiriveta section (2) Mas de Faro (3) La Roca section. Main paleoflow directions indicated in orange (from Nijman and Puigdefabregas, 1978). Regional map after Teixell (1998).**



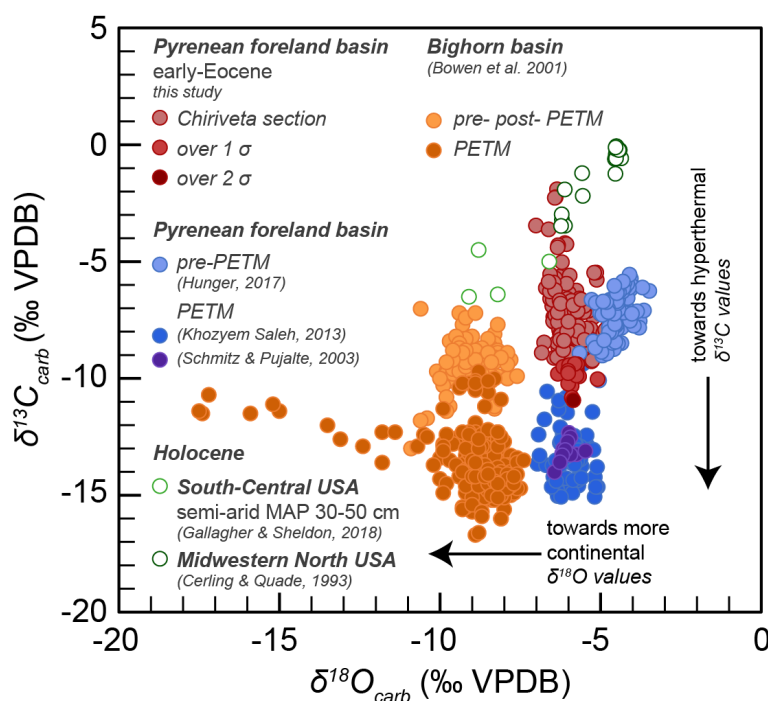
710 **Figure 3:** A - Time constraints on the Castissent Fm. MP zone from the continental section from Checa-Soler (2004) and Payros and Tosquella (2009). SBZ and NP in the Campo section from (Kapellos and Schaub, 1973; Schaub, 1966, 1981; Tosquella, 1995), magnetostratigraphy from Bentham and Burbank (1996). SBZ in El Pueyo from Payros and Tosquella (2009). Magnetostratigraphy in El Pueyo from Poyatos-Moré (2014). B – Extended map of the study area. For map legend and references, see Fig. 2.



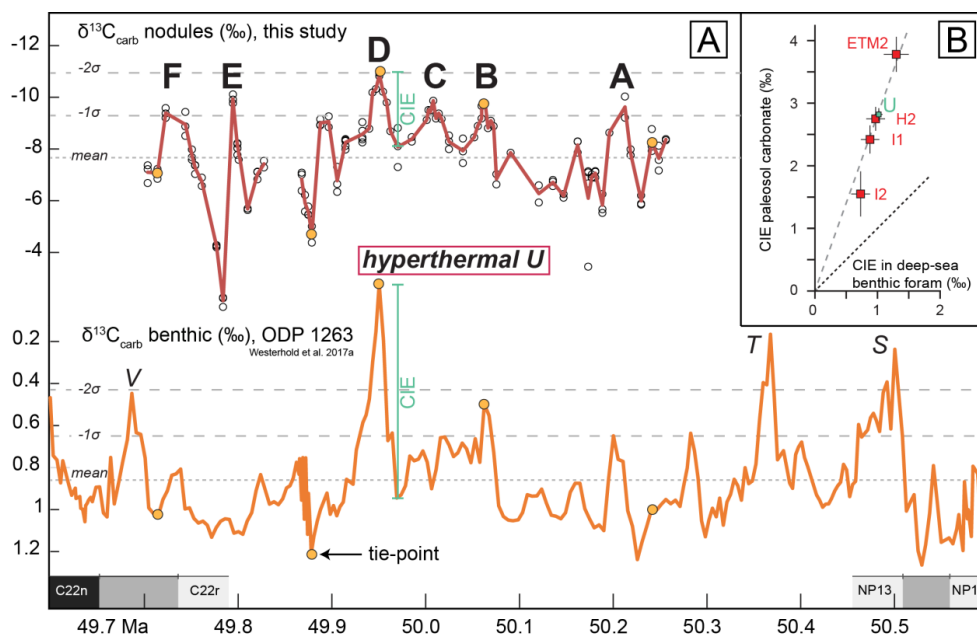
715 **Figure 4: Field images of the Chiriveta section (42°7'56.57"N, 0°41'19.45"E).** A – Outcrop view of Members A and B
of the Castissent Formation. B – Close-up view of the upper part of Castissent A Member. Fluvial channel-fill
deposits, intercalated in reddish floodplain and overbank deposits and regional marine incursions (M1). C – M0, first
720 marine incursion at the base of the Castissent Fm described by Marzo et al. (1988) expressed in the Chiriveta section
by a tidal-influenced coarse sandstone with herringbone cross-stratification. D – Yellow mottled paleosol between
NCIE C and D. E – Red floodplain interval equivalent of the NCIE C. F – 2 m-thick grey interval interpreted as poorly
drained brackish water facies and equivalent to the marine incursion M1. G – ~6m thick laterally extensive Castissent
B sandbody incised in the underlying floodplain deposits. H – Mottled silt, interpreted as pedogenetic fluvial channel
overbank deposits.



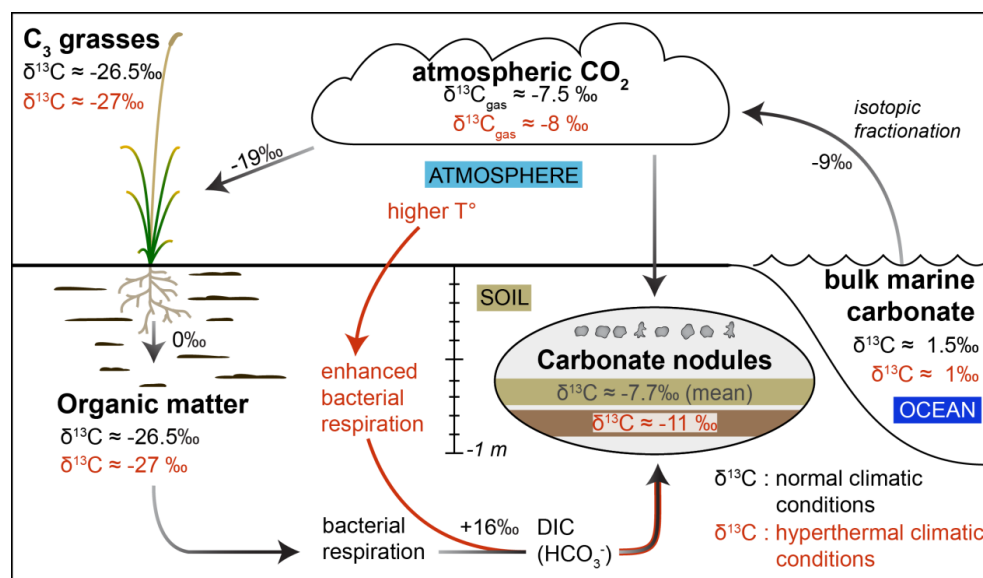
725 **Figure 5: Isotopic and geochemical data from the Chiriveta section. For the isotope dataset, the curves pass through the mean values at each sample position. Samples with minimum in $\delta^{13}\text{C}$ values below 1 and 2 standard deviation are labelled A to F. Mean Annual Precipitation (MAP) was estimated from the empirical relationship between MAP and CaO to Al_2O_3 ratio (Sheldon et al., 2002).**



730 **Figure 6: Continental $\delta^{13}\text{C}$ and $\delta^{18}\text{O}$ values from the early Eocene Castissent Fm in the Chiriveta section (this study) plotted with pre- and syn-PETM $\delta^{13}\text{C}$ and $\delta^{18}\text{O}$ values from the same area (Hunger, 2018; Khozyem Saleh, 2013) and Pre-, syn and post-PETM values from the Bighorn Basin (Bowen et al., 2001) as well as recent pedogenic carbonate isotopic values (Cerling and Quade, 1993; Gallagher and Sheldon, 2016).**



735 **Figure 7:** A - Scaling of the Chiriveta isotopic section with the time equivalent interval of site 1263 (Westerhold et al., 2017). The correlation was calculated using the Analyseries software (Paillard et al., 1996) and centred on NCIE D and hyperthermal U. Mean, minus 1 and 2 SD lines on the global record were calculated sets over the selected time period. The correlation coefficient (r) between the two curves is 0.65. B - Hyperthermal U amplitude in paleosol carbonate and benthic foraminifera (inset B after Abels et al. (2016))



740 **Figure 8:** Components influencing the $\delta^{13}\text{C}$ values of pedogenic carbonate nodules. Mean early Eocene bulk marine carbonate and small scale hyperthermal (all except PETM) are from Westerhold et al. (2018). Fractionation value between organic matter and carbonate nodules are based on Sheldon and Tabor (2009). All other fractionation values are based on Koch et al. (1995). Mean carbonate nodule values come from this study.

745